Published online 19 June 2023

Nucleic Acids Research, 2023, Vol. 51, No. 14 ***7649–7665***
https://doi.org/10.1093/nar/gkad525

Structural and biochemical insights into the molecular mechanism of TRPT1 for nucleic acid ADP-ribosylation

Xiaoyun Yang [1,2,†], Jiaxu Wang [1,†], Simin Li [1,†], Xiaobing Li [1], Jingjing Gong [1], Zhenzhen Yan [1], Huan Zhou [3], Chen Wu [1,*] and Xiuhua Liu [1,*]

[1]College of Life Sciences, Hebei Innovation Center for Bioengineering and Biotechnology, Institute of Life Sciences and Green Development, Hebei University, Baoding 071002, Hebei, China, [2]School of Life Sciences, Southern University of Science and Technology, Shenzhen 518055, Guangdong, China and [3]Shanghai Synchrotron Radiation Facility, Shanghai Advanced Research Institute, Chinese Academy of Sciences, Shanghai 201204, China

Received September 30, 2022; Editorial Decision May 27, 2023; Accepted June 06, 2023

ABSTRACT

Nucleic acid ADP-ribosylation has been established as a novel modification found in a wide diversity of prokaryotic and eukaryotic organisms. tRNA 2′-phosphotransferase 1 (TRPT1/TPT1/KptA) possesses ADP-ribosyltransferase (ART) activity and is able to ADP-ribosylate nucleic acids. However, the underlying molecular mechanism remains elusive. Here, we determined crystal structures of TRPT1s in complex with NAD+ from *Homo sapiens*, *Mus musculus* and *Saccharomyces cerevisiae*. Our results revealed that the eukaryotic TRPT1s adopt common mechanisms for both NAD+ and nucleic acid substrate binding. The conserved SGR motif induces a significant conformational change in the donor loop upon NAD+ binding to facilitate the catalytic reaction of ART. Moreover, the nucleic acid-binding residue redundancy provides structural flexibility to accommodate different nucleic acid substrates. Mutational assays revealed that TRPT1s employ different catalytic and nucleic acid-binding residues to perform nucleic acid ADP-ribosylation and RNA 2′-phosphotransferase activities. Finally, cellular assays revealed that the mammalian TRPT1 is able to promote endocervical HeLa cell survival and proliferation. Together, our results provide structural and biochemical insights into the molecular mechanism of TRPT1 for nucleic acid ADP-ribosylation.

GRAPHICAL ABSTRACT

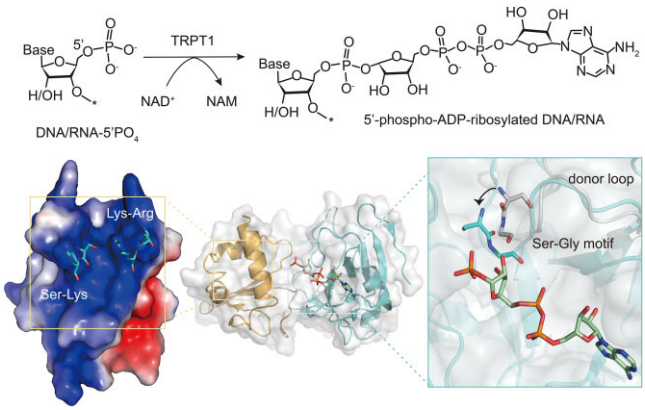

INTRODUCTION

ADP-ribosylation is a canonical post-translational modification targeting macromolecules and plays a significant role in regulating many biological processes including DNA damage repair, chromatin remodeling, host–virus interactions, RNA metabolism, apoptosis and cytoplasmic stress responses (1–3). The chemical process of ADP-ribosylation is involved in transferring the ADP-ribose moiety from the NAD+ donor onto target substrates, simultaneously releasing nicotinamide (4). The enzymes catalyzing ADP-ribosylation belong to the ADP-ribosyltransferase (ART) superfamily (5), which is divided into cholera toxin-like ART (ARTC) and poly(ADP)-ribose polymerase (PARP; also known as diphtheria toxin-like ART, ARTD) subfamilies (6,7). PARPs, sharing the conserved ART domain, are the most intensively studied ARTs and consist of 17 members in human cells (2).

*To whom correspondence should be addressed. Tel: +86 133 1523 5028; Fax: +86 0312 5079364; Email: liuxiuhua_2004@163.com
Correspondence may also be addressed to Chen Wu. Tel: +86 139 0312 9899; Fax: +86 0312 5079364; Email: wuchen@hbu.deu.cn
†The authors wish it to be known that, in their opinion, the first three authors should be regarded as Joint First Authors.

Over the years, the well-studied ADP-ribosylation was thought to be a unique covalent modification of protein targets (1,8). Recently, striking discoveries have been established nucleic acids—DNA and RNA—as novel ADP-ribosylation substrates which are found in a wide diversity of prokaryotic and eukaryotic organisms, generating a new exciting field termed DNA and RNA ADP-ribosylation carried out by specific ARTs (1,9–11). In mammals, several PARP family members, such as PARP1–PARP3, and PARP10, PARP11 and PARP15, have been shown to possess DNA and RNA ADP-ribosylation activity and exhibit diverse nucleic acid substrate preferences *in vitro* (9,10,12).

Additionally, tRNA 2′-phosphotransferase 1 (TRPT1/TPT1/KptA), a PARP-like protein, is capable of catalyzing the transfer of the ADP-ribose moiety from NAD^+ to the 5′-terminal phosphates of single-stranded RNA (ssRNA) and ssDNA substrates, independent of oligomer length (1,9,13). The TRPT1/TPT1/KptA family was initially found in *Saccharomyces cerevisiae* and was shown to be as an essential RNA 2′-phosphotransferase in the fungal tRNA splicing pathway, which typically forming a 2′-PO_4, 3′–5′ phosphodiester splice junction in the tRNA ligation reaction (14–16). The human version and those of its close relatives are referred to as TRPT1, and the yeast and bacterial versions of TRPT1 are known as TPT1 and KptA, respectively. In *S. cerevisiae*, TPT1 plays an essential role in the final step of tRNA splicing by transferring the internal 2′-phosphate in the splicing junction to NAD^+ via a two-step reaction to generate 2′-OH RNA and ADP-ribose-1″,2″-cyclic phosphate, which is finally hydrolyzed to ADP-ribose-1″-phosphate (ADPRp) (17,18). The TPT1 homologous proteins are evolutionarily conserved in bacterial, archaeal and eukaryotic species, yet many do not have known pathways to form RNAs containing internal 2′-phosphate and/or intron-containing tRNAs (13,18). Instead, the TPT1 homologs are able to ADP-ribosylate nucleic acids, suggesting that nucleic acid ADP-ribosylation may be a conserved enzyme activity of TRPT1/KptA/TPT1 family members across all domains of life (1,9,11,13). Weixler *et al*. recently identified the nucleic acid ADP-ribosylation catalyzed by TRPT1 and PARPs in human cells, and found that multiple cellular stressors can mediate the nucleic acid ADP-ribosylation in human cells (11). In addition, Tromans-Coia *et al*. demonstrated ADP-ribosylation on genomic DNA in human cells (19). However, the detailed molecular mechanism of TRPT1-dependent nucleic acid ADP-ribosylation remains elusive and the catalytic differences between nucleic acid ADP-ribosylation and RNA 2′-phosphotransferase of TRPT1 are unclear.

Herein, we determined the crystal structures of three TRPT1s in complex with NAD^+ from *Homo sapiens* (HsTRPT1), *Mus musculus* (MmTRPT1) and *S. cerevisiae* (ScTRPT1). Our structural analysis, combining *in vitro* biochemical assays, revealed the NAD^+ recognition pattern among MmTRPT1, HsTRPT1 and ScTRPT1. Furthermore, we also displayed the nucleic acid substrate binding mode and mapped the catalytic-related residue diversities between ART and 2′-phosphotransferase activities. We additionally found that HsTRPT1 is associated with endocervical HeLa cell survival and proliferation. Together, our study provides structural and biochemical insights into the molecular mechanism of TRPT1 on nucleic acid ADP-ribosylation.

MATERIALS AND METHODS

Cloning and plasmid constructs

The DNA sequences encoding full-length HsTRPT1 isoform 1 (residues 1–253), MmTRPT1 (residues 1–249) and ScTRPT1 (residues 1–230) were synthesized with codon optimization (Genscript, China), and amplified by polymerase chain reaction (PCR) using oligonucleotide primers with the restriction recognition sites BamHI and XhoI located at the 5′ and 3′ ends, and then subcloned into the modified pET-15b vector, which carries an N-terminal hexa-histidine tag and a cleavage site for human rhinovirus 3C (HRV 3C) protease (Supplementary Figure S1), using standard molecular biology techniques. The corresponding optimized full-length sequences are listed in Supplementary Table S1. Based on the structural analysis of TRPT1–ADPRp complexes and the $ScTRPT1^{NAD\ lobe}$–NAD^+ complex, a series of mutants were generated using standard molecular biology techniques. The optimized wild-type HsTRPT1 open reading frames (ORFs) were cloned into the pEGFP-C1 vector.

Protein expression and purification

Escherichia coli BL21-Codon plus (DE3) cells carrying the recombinant plasmid pET-15b-MmTRPT1/HsTRPT1/ScTRPT1 were grown in Luria–Bertani (LB) broth medium at 37°C to an OD_{600} of 0.7–0.9. Then 0.1 mM isopropyl-β-D-1-thiogalactopyranoside (IPTG) was supplemented to induce the recombinant protein expression at 16°C for 15 h. Cells were harvested by centrifugation at 10 000 *g* for 10 min and resuspended in ice-cold lysis buffer [25 mM Tris–HCl pH 8.0, 500 mM NaCl and 5% (v/v) glycerol]. The cells were lysed through sonication, and the cell lysate was centrifuged at 35 000 *g* for 40 min.

The supernatant containing soluble MmTRPT1/HsTRPT1/ScTRPT1 was loaded onto a nickel-chelating Sepharose (GE Healthcare) column pre-equilibrated with lysis buffer. After extensive washing with lysis buffer supplemented with 10 mM imidazole, all bound protein was eluted using elution buffer [25 mM Tris–HCl pH 8.0, 500 mM NaCl, 5% (v/v) glycerol and 250 mM imidazole]. The recombinant proteins were incubated with HRV 3C protease at a molar ratio of 100:1 and dialyzed overnight at 4°C against the buffer [25 mM Tris–HCl pH 8.0, 150 mM NaCl, 5% (v/v) glycerol, 1 mM dithiothreitol (DTT)]. Then, the recombinant protein was further purified with a cation-exchange column (Hi-Trap SP HP column, GE Healthcare) and eluted using a 150 ml linear gradient of 0.1–1 M NaCl. Finally, the protein MmTRPT1/HsTRPT1/ScTRPT1 was purified using a Superdex 200 Increase column (GE Healthcare) in 25 mM Tris–HCl pH 8.0, 150 mM NaCl and 1 mM DTT.

For the purification of wild-type and mutant proteins used in the biochemical experiments, the cells were lysed in resuspension buffer [25 mM Tris–HCl pH 8.0, 1 M NaCl,

5% (v/v) glycerol], and TRPT1 proteins were purified by a nickel-chelating Sepharose (GE Healthcare) column using elution buffer containing 1 M NaCl to eliminate nucleic acid contaminants. Then TRPT1 wild-type and mutant proteins were purified using the same procedure as described above.

Crystallization, data collection and processing

To screen for crystallization of the MmTRPT1/HsTRPT1/ScTRPT1 and NAD^+ complex, TRPT1s and NAD^+ (Sigma) were mixed in the molar ratio of 1:1.5 and then incubated on ice for 30 min before crystallization. Preliminary crystallization was carried out using the sitting-drop vapor diffusion method at 18°C by mixing 1 μl of TRPT1–NAD^+ complex and 1 μl of reservoir solution. After optimization, the best crystals of the MmTRPT1–NAD^+ complex were obtained in the reservoir solution containing 0.04 M potassium phosphate dibasic, 16% (w/v) polyethylene glycol (PEG) 8000 and 0.2% (w/v) D-sorbitol, the best crystals of the HsTRPT1–NAD^+ complex were obtained in the reservoir solution consisting of 0.1 M Tris–HCl pH 8.5 and 25% (w/v) PEG 3350, and the best crystals of the ScTRPT1–NAD^+ complex were grown in the reservoir solution containing 0.1 M Tris–HCl pH 8.5 and 1.4 M ammonium tartrate dibasic.

To collect X-ray diffraction data, the crystals were immersed in the cryoprotectant buffer consisting of reservoir solution and 20% (v/v) glycerol, and then flash-frozen in liquid nitrogen. X-ray diffraction data were collected at Shanghai Synchrotron Radiation Facility (SSRF), beamline BL19U1. The crystal of the MmTRPT1–NAD^+ complex belongs to space group P3121 with the unit cell dimensions $a = 65.5$ Å, $b = 65.6$ Å, $c = 148.5$ Å and $\beta = 90.00°$. The crystal of the HsTRPT1–NAD^+ complex belongs to space group I222 with the unit cell dimensions $a = 53.9$ Å, $b = 84.1$ Å, $c = 101.5$ Å and $\beta = 90.00°$. The crystal of the ScTRPT1–NAD^+ complex belongs to space group P3221 with the unit cell dimensions $a = 41.7$ Å, $b = 41.7$ Å, $c = 129.1$ Å and $\beta = 90.00°$. All datasets were processed using the XDS software package (20).

Structure determination and refinement

The crystal structure of MmTRPT1/HsTRPT1/ScTRPT1–NAD^+ was solved through molecular replacement using the Phaser program in the CCP4 software suite (21). The structure of CthTPT1 (PDB code: 6E3A) was used as the search model. PHENIX (22) and COOT (23) were used, respectively, for further manual model building and refinement. All data collection and structure refinement statistics are summarized in Supplementary Table S2. All the molecular graphics are generated using PyMOL (http://www.pymol.org). All protein electrostatic potential surfaces are calculated using the APBS module in PyMOL (version 2.5.4) (24).

Molecular dynamics simulations

Molecular dynamics (MD) simulations of HsTRPT1, MmTRPT1, ScTRPT1 and their respective complexes with ligands were performed using the GROMACS package (25). Antechamber in AMBER tool, ACPYPE and AMBER99SB-ILDN force field were applied for the ligands and TRPT1s in the MD simulation processes (26). All systems were centered in a cube and dissolved with TIP3P waters. Sodium and chloride ions were added to neutralize the electric charge. The particle mesh Ewald method was used to compute the electrostatic interactions with a real-space cut-off distance of 1 nm, and the van der Waals interactions were set at the same cut-off value. These systems were energy minimized and heated to 25°C before the production process. The trajectory production processes proceeded for 200 ns, and the root-mean-square deviations (RMSDs) and fluctuations (RMSFs) were calculated on the Cα atoms of each residue.

In vitro ADP-ribosylation assay

The non-radioactive nucleic acid ADP-ribosylation assay was performed as described previously for Cyanine3-labeled RNA ADP-ribosylation (9). The ssRNA and ssDNA oligonucleotides used in this study were chemically synthesized from Genescript, and the sequences are listed in Supplementary Table S3. All buffers were prepared using DNase/RNase-free water and sterilized using a 0.22 μm filter. The 10 μl reaction mixture consists of 20 mM Tris–HCl pH 8.0, 50 mM NaCl, 0.5 mM NAD^+, 5 mM $MgCl_2$ and 1 mM DTT. Protein (1 μM) was added along with nucleic acid substrate at the final concentration of 0.5 μM (the stock concentration is 10 μM, Cyanine3 labeled) per reaction. After incubation at 1 h in room temperature, reactions were quenched by adding 0.15% sodium dodecylsulfate (SDS) and 0.5 U of protease K (NEB) and incubating at 37°C for 30 min. Samples were loaded on the denaturing urea–polyacrylamide gel electrophoresis (PAGE) gel consisting of 25% (w/v) polyacrylamide, 8 M urea and 1× TBE. Gels were run at 300 V (~25 mA starting current) for 45 min and finally visualized using the Bio-Rad ChemiDoc™ MP imaging system for the Cyanine3 fluorophore. All ADP-ribosylation assays were independently repeated three times.

Isothermal titration calorimetry

Isothermal titration calorimetry (ITC) experiments were performed to quantify the binding affinity between wild-type TRPT1 or its mutants and NAD^+ (or 21 nt ssDNA) using Microcal PEAQ-ITC (Malvern Panalytical). All titrations were carried out in buffer containing 20 mM Tris–HCl pH 8.0 and 150 mM NaCl. To measure the binding affinity between protein and NAD^+, 2–3 mM NAD^+ was injected into the calorimetric cell containing 30–50 μM wild-type TRPT1 or its mutants. To determine the binding affinity between the 21 nt ssDNA and wild-type TRPT1, 300 μM 21 nt ssDNA was injected into the calorimetric cell containing 25–30 μM wild-type TRPT1. All titrations were carried out at 25°C and were initiated by a 0.4 μl pre-injection, and followed by sequential 18 × 2 μl injections at 150 s intervals. The data were analyzed using Microcal PEAQ-ITC analysis software. All ITC assays were independently repeated three times.

Complementation of *ScTrpt1*Δ by HsTRPT1/MmTRPT1 mutants in *S. cerevisiae*

For functional complementation of *ScTrpt1*Δ in *S. cerevisiae*, the *ScTrpt1*Δ haploid strain YBS501 (*MATa ura3-1 ade2-1 trp1-1 his3-11,15 leu2-3,11 can1-100 trpt1::LEU2* p416-ScTRPT1), in which the *Trpt1* ORF was deleted and replaced by *LEU2*, is dependent for viability on the plasmid p416 (*CEN URA3 ScTRPT1*) (18,27,28). We generated plasmids p414 (*CEN TRP*) encoding wild-type MmTRPT1, HsTRPT1 and their mutants under the control of the constitutive *ScTRPT1* promoter, and transformed them separately into YBS501 cells. The individual TRP^+ colonies from each transformation were patched to $TRP^|$ agar medium and cells from each isolate were then spotted on agar medium supplemented with 0.75 mg/ml 5-FOA (5-fluoroorotic acid). The plates were incubated at 30°C. The MmTRPT1/HsTRPT1 mutants, which are unable to form 5-FOA-resistant colonies after 8 days, are considered as lethal *in vivo*. Viable FOA-resistant colonies were then grown in YPD-Ad (1% yeast extract, 2% peptone, 2% dextrose, 0.1 mg/ml adenine) liquid medium at 30°C to mid-log phase (OD_{600} of 0.4–0.6), and diluted to attain an OD_{600} of 0.1, and aliquots (3 μl) of serial 5-fold dilutions were spotted on YPD agar plates and incubated at 20, 25, 30, 34 and 37°C.

Cell culture and antibodies

HEK-293T, HeLa, C-33A and human cervical epithelial cells (ATCC, catalog nummber: PCS-480–011) were maintained in Dulbecco's modified Eagle's medium (DMEM) containing 10% fetal bovine serum (FBS) in a humidified incubator with 5% CO_2 (v/v) at 37°C. The primary antibodies were used as follows: anti-TRPT1 antibody (PA5-58504, Invitrogen, RRID: AB_2648978), anti-β-actin antibody (60009–1-Ig, Proteintech, RRID: AB_2687938) and anti-green fluorescent protein (GFP) antibody (66002–1-Ig, Proteintech, RRID: AB_11182611).

Establishment of a TRPT1 knockdown HeLa cell line

The short hairpin RNA (shRNA) sequences used for TRPT1 knockdown (KD) were as follows: shRNA1: 5′-GCGGTCCCATTGTGAAATAGC-3′ and shRNA2: 5′-GGCCATCCATCCTACTCAAAG-3′. Both shRNA1 and shRNA2 were cloned separately into the lentiviral vector pLKO.1. To generate lentivirus, HEK-293T cells (~1×10^6) were cultured in 6 cm dishes the day before transfection. Then the HEK-293T cells were co-transfected with the plasmids (3 μg of pLKO.1, 2 μg of pxPAX2 and 1 μg of pMD2.G) using 12 μl of Lipofectamine 2000 reagent mixed in 500 μl of Opti-MEM™ I Reduced Serum Medium (Gibco). After 48 h of incubation, the packaged virus was harvested to infect HeLa cells. TRPT1 KD HeLa cells were screened with 2.5 μg/ml puromycin (Sigma) for 1 week after lentivirus infection. The TRPT1 KD efficiency was validated by western blot.

Western blot analysis

The cells were washed with 1× phosphate-buffered saline (PBS) buffer three times and lysed with NETN-300 buffer (20 mM Tris–HCl, pH 8.0, 300 mM NaCl, 0.5% Nonidet P-40, 2 mM EDTA). Equal amounts of samples were loaded and separated by 12% SDS–PAGE and then transferred onto a polyvinylidene fluoride (PVDF) membrane. The membranes were then blocked with 5% skimmed milk in TBST (Tris-buffered saline–Tween) buffer and probed with anti-TRPT1 antibody according to the standard protocol, and then the same membrane was stripped and re-probed with anti-β-actin antibody. The blots were visualized using an enhanced chemiluminescence reagent kit and analyzed using ChemiDoc™ MP Imaging System (Bio-Rad, CA, USA). β-Actin was used as a loading control.

Cell counting kit-8 (CCK-8) assay

Cells (~3×10^5/well) were seeded into 6-well plates. After 12 h of incubation, cells were transfected with 1 μg of plasmid using 2 μl of Lipofectamine 2000. Almost 24 h later, the cells were re-seeded into 96-well plates with an initial density of ~2.5×10^3 cells/well. After seeding for 24, 48, 72 and 96 h, cells were incubated with the CCK-8 assay reagent (K1018, Apexbio, USA) at 37°C for 1 h according to the manufacturer's instruction. The optical density (OD) values were measured using Thermo Scientific Multiskan GO at the wavelength of 450 nm. The experiments were performed in triplicate.

Colony formation assay

TRPT1 KD cells were transfected with pEGFP-C1 plasmid containing wild-type HsTRPT1. After 24 h, cells were re-seeded onto 6-well plates at a density of 0.8×10^3/well and cultured for 10–14 days until visible colonies formed. After washing with 1× PBS, the cells were further fixed using methanol, and stained with Giemsa dye. The cell viability was calculated by the ratio of the colony number and seeded cell number, normalized by the untreated group. The experiments were carried out in triplicate. The Shapiro–Wilk test in IBM SPSS Statistics (version 26.0) was used to check the normal distribution of the colony formation data. One-way analysis of variance (ANOVA) was employed to carry out multiple comparisons.

In silico analysis

UALCAN (http://ualcan.path.uab.edu) is an interactive and comprehensive web portal for analyzing cancer OMICS data [The Cancer Genome Atlas (TCGA), MET500, CPTAC and CBTTC] (29). In this study, we used the UALCAN web portal to perform pan-cancer analysis of the TRPT1 expression level in 12 cancer types with paired normal samples through the RNA sequencing data in the TCGA dataset. cBioPortal (http://www.cbioportal.org) was used to analyze the genomic alteration profiles of TRPT1 in TCGA database.

RESULTS

Overall structure of the TRPT1–NAD^+ complex from *Homo sapiens* and *Mus musculus*

Recent studies have reported that HsTRPT1 and several bacterial TRPT1 enzymes are capable of ADP-ribosylating

ssRNA and ssDNA (1,9,13). Here, we surveyed MmTRPT1 and ScTRPT1 for their ADP-ribosylation activities towards ssRNA and ssDNA oligomers with 5′ or 3′ phosphate ends or without a phosphate group (noP). Consistent with HsTRPT1, both MmTRPT1 and ScTRPT1 can effectively ADP-ribosylate ssDNA and ssRNA with a 5′-PO_4 end, less efficiently for ssDNA and ssRNA with a 3′-PO_4 end and were inactive for non-phosphorylated nucleic acids (Figure 1A). Additionally, in the conditions tested, HsTRPT1 and MmTRPT1 exhibit comparable levels of ADP-ribosylation activity towards ssDNA, while ScTRPT1 exhibits relatively low activity (Figure 1A). Together, these biochemical data suggest that TRPT1s represent phosphate-dependent ART activity preferentially towards ssDNA or ssRNA with a 5′-PO_4 end.

To demonstrate the molecular mechanism underlying nucleic acid ADP-ribosylation of TRPT1s, we crystallized native HsTRPT1, MmTRPT1 and their respective complexes with NAD^+. However, the attempts to crystallize the native HsTRPT1 and MmTRPT1 were unsuccessful and we only determined the crystal structures of HsTRPT1 and MmTRPT1 in complex with NAD^+. The final model of the HsTRPT1/MmTRPT1–NAD^+ complex contains one TRPT1 molecule in the asymmetric unit. The electron density map clearly showed that one ADPRp molecule, the final by-product of the tRNA 2′-phosphotransferase 1 activity of TRPT1s, binds to the HsTRPT1/MmTRPT1 monomer (Figure 1B, C, D). It has been reported that one ADPRp molecule also binds to the TPT1 from *Clostridium thermocellum* (CthTPT1) in the crystal structure (18); structural superposition reveals that HsTRPT1/MmTRPT1 binds the ADPRp molecule in a similar pattern to that shown in the CthTPT1–ADPRp complex (PDB code: 6E3A) (Supplementary Figure S2).

The HsTRPT1 and MmTRPT1 models include residues 25–230 and residues 19–224, respectively. No electron density is observed for both N- and C-terminal regions (residues 1–24 and 231–253 for HsTRPT1, residues 1–18 and 225–249 for MmTRPT1). Both TRPT1 structures contain 5 α-helices and 13 β-strands, and can be divided into an N-terminal RNA lobe (residues 25′–102′ and residues 19–97, where ′ indicates the corresponding residue in HsTRPT1 and residues without label belong to MmTRPT1) and a C-terminal NAD^+ lobe (residues 116′–229′ and residues 111–224) (Figure 1B, C). The two domains are connected by a 13 amino acid long loop (termed the linker loop, corresponding to residues 103′–115′ and residues 98–110, respectively) (Figure 1B).

The overall architectures of HsTRPT1 and MmTRPT1 are very similar to each other, with an RMSD value of 1.022 Å for 190 matched Cα atoms (Figure 1C). Structural alignment using the DALI server suggests that the closest homologs of both TRPT1s are tRNA 2′-phosphotransferase from *Aeropyrum pernix* (ApeTPT1) (PDB code: 1WFX) (30) and CthTPT1 (PDB code: 6E3A) (18). Structural superposition shows that the major conformational variation among them occurs in the β7–β8 loop (residues 156′–174′ and residues 151–169), which is situated in the NAD^+ lobe of both TRPT1s, corresponding to the Ala128–Pro144 loop and the Leu121–Val139 loop in CthTPT1 and ApeTPT1, respectively. In contrast, both loops contain an inserted 10 residue α-helix secondary structure in CthTPT1 and ApeTPT1, highlighting the high flexibility of the β7–β8 loop (termed donor loop) in HsTRPT1 and MmTRPT1 (Supplementary Figure S3). The conformational diversity in the donor loop is probably associated with their distinct features in the NAD^+ binding mode.

NAD^+ recognition in HsTRPT1 and MmTRPT1

ITC assays were performed to quantify the binding affinity between TRPT1s and NAD^+. The results showed that the dissociation constant (K_d) between HsTRPT1 and NAD^+ is 11.8 ± 0.32 μM with 1:1 stoichiometric binding, and the K_d is 22.3 ± 0.75 μM between MmTRPT1 and NAD^+. In addition, the K_d is 23.8 ± 1.88 μM for NAD^+ bound to ScTRPT1, indicating that TRPT1 from different species exhibits an equivalent capacity for NAD^+ binding (Figure 2A; Supplementary Table S4A).

The NAD^+-binding pocket is long and shallow, fully exposed on the surface of the NAD^+ lobe, and numerous hydrogen bonds are involved in the interaction between NAD^+ and MmTRPT1/HsTRPT1 (Figure 2B). The adenine ring is sandwiched by the Ile135–Gln143/Ile140′–Gln148′ pair, and several hydrogen bonds are involved in the adenine specificity. In detail, adenine-N1, adenine-N6 and adenine-N7 form hydrogen bonds with Ser134/Ser139′, Gly139/Gly144′ and Ser141/Ser146′, respectively. The adenosine ribose 2′-OH forms bifurcated hydrogen bonds with His125/His130′ and Thr127/Thr132′ from the HGT motif, which is conserved among all TRPT1 family members (18,27,31). The adenosine ribose 3′-OH is bridged to the β-phosphate via a water molecule (named W1), which in turn forms a hydrogen bond with the carbonyl group of glycine (Gly126/Gly131′) from the HGT motif. The diphosphate moiety is stabilized directly by Arg145/Arg150′ and Arg165/Arg170′ via hydrogen bonds (Figure 2B). In addition, Arg142/Cys147′ and Gly144/Gly149′ form water-mediated hydrogen bonds with the α-phosphate. The distal ribose 2′′-OH also forms hydrogen bonds with Ser162/Ser167′ and Gly163/Gly168′, and the 1′′-PO_4 of the distal ribose is stabilized by Arg35/Arg40′, Lys79/Lys84′ and Arg81/Arg86′ through electrostatic interactions. Multiple sequence alignment and structural comparison revealed that the NAD^+-binding residues in MmTRPT1 and HsTRPT1 are highly conserved in other TRPT1 homologs (Figures 2B and 3D), indicating a common mode of NAD^+ bound to TRPT1 members.

To corroborate our structural analysis, a series of mutations were generated in the NAD^+-binding pockets of MmTRPT1 and HsTRPT1. We examined the binding affinity constants of NAD^+ and these recombinant mutants using ITC assays. Compared with the wild-type TRPT1s, the mutants H125A–T127A/H130′A–T132′A, I135A–Q143A/I141′A–Q148′A and R145A/R150′A had no binding activity towards NAD^+, suggesting that these residues are essential for the binding of NAD^+ (Figure 2C; see also Supplementary Figure S4 and Supplementary Table S4A). These mutants also lacked the enzymatic activities for ssRNA and ssDNA ADP-ribosylation, revealing that the interactions with the adenine and adenosine ribose moieties of NAD^+ are essential for the nucleic acid

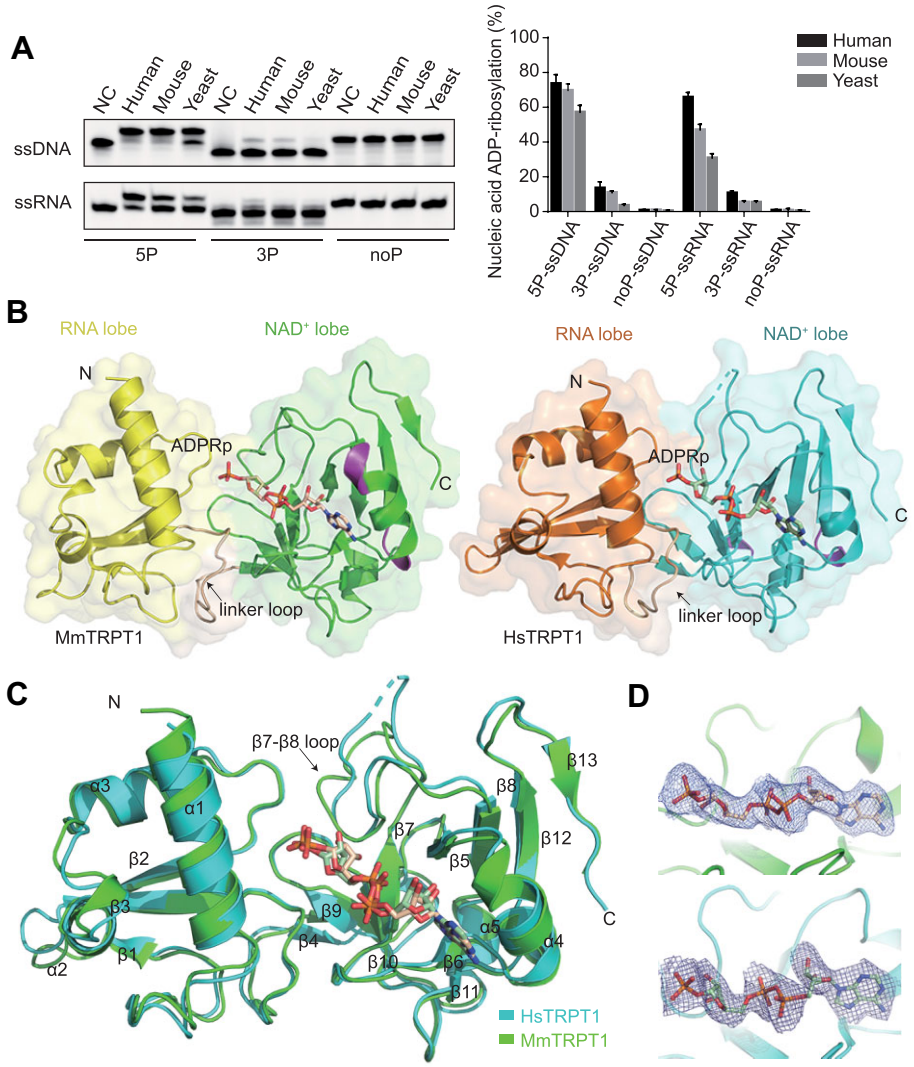

Figure 1. Overall structures of the TRPT1s bound to ADPRp. (**A**) TRPT1s exhibit phosphate-dependent ADP-ribosylation activities towards ssDNA or ssRNA with a 5′-PO_4 end. The nucleic acid substrates and products are indicated as the lower and upper bands, respectively. NC, negative control; human, HsTRPT1; mouse, MmTRPT1; yeast, ScTRPT1. (**B**) Cartoon representation of the crystal structures of MmTRPT1–ADPRp (left panel) and HsTRPT1–ADPRp complexes (right panel). The N-terminal domain, termed the RNA lobe, resembles the winged-helix protein fold. The C-terminal domain, named the NAD^+ lobe, represents a mixed α/β fold. The RNA lobe and NAD^+ lobe in MmTRPT1 are displayed in yellow and green, respectively. The RNA lobe and NAD^+ lobe in HsTRPT1 are shown in orange and cyan, respectively. The linker loop is rendered as beige and the 3_{10} α-helix is rendered as magenta. The ligand ADPRp is depicted as a stick. (**C**) Structural superimposition of MmTRPT1–ADPRp (green) and HsTRPT1–ADPRp complexes (cyan). Both TRPT1 structures contain 5 α-helices and 13 β-strands. The β7–β8 loop contributing to NAD^+ binding is labeled. (**D**) The 2*Fo*–*Fc* map for the ADPRp ligand in the active site of MmTRPT1/HsTRPT1 contoured at 0.5 σ.

ADP-ribosylation (Figure 2D; Supplementary Figure S5A). In contrast, the mutants R35A/R40′A, K79A/K84′A and R81A/R86′A can also bind to NAD^+ with similar binding affinity to that of wild-type TRPT1, indicating that residues Arg35/Arg40′, Lys79/Lys84′ and Arg81/Arg86′ are not required for the NAD^+ binding (Figure 2C; Supplementary Figure S4; Supplementary Table S4A).

Overall structure of the ScTRPT1–NAD^+ complex

The enzymatic activity of ScTRPT1 on nucleic acid ADP-ribosylation was less than that of MmTRPT1 and HsTRPT1 according to our *in vitro* assay results (Figure 1A). To demonstrate the differences in mechanisms on ADP-ribosylation activities, we used the full-length ScTRPT1 bound to NAD^+ for crystallization. The final model of the ScTRPT1–NAD^+ complex contains one protein molecule and one NAD^+ molecule in the asymmetric unit (Figure 3A, B). Unexpectedly, the ScTRPT1 monomer only contains residues 101–230 based on the electron density map, corresponding to the C-terminal NAD^+ lobe of MmTRPT1 and HsTRPT1 (for simplicity, the crystal structure of the degraded ScTRPT1 fragment was termed $ScTRPT1^{NAD\ lobe}$). Structural superimposition revealed that the RMSD values of $ScTRPT1^{NAD\ lobe}$ and MmTRPT1/HsTRPT1 are 0.729 Å/0.951 Å for 61/69 matched Ca atoms, suggesting a high similarity among the

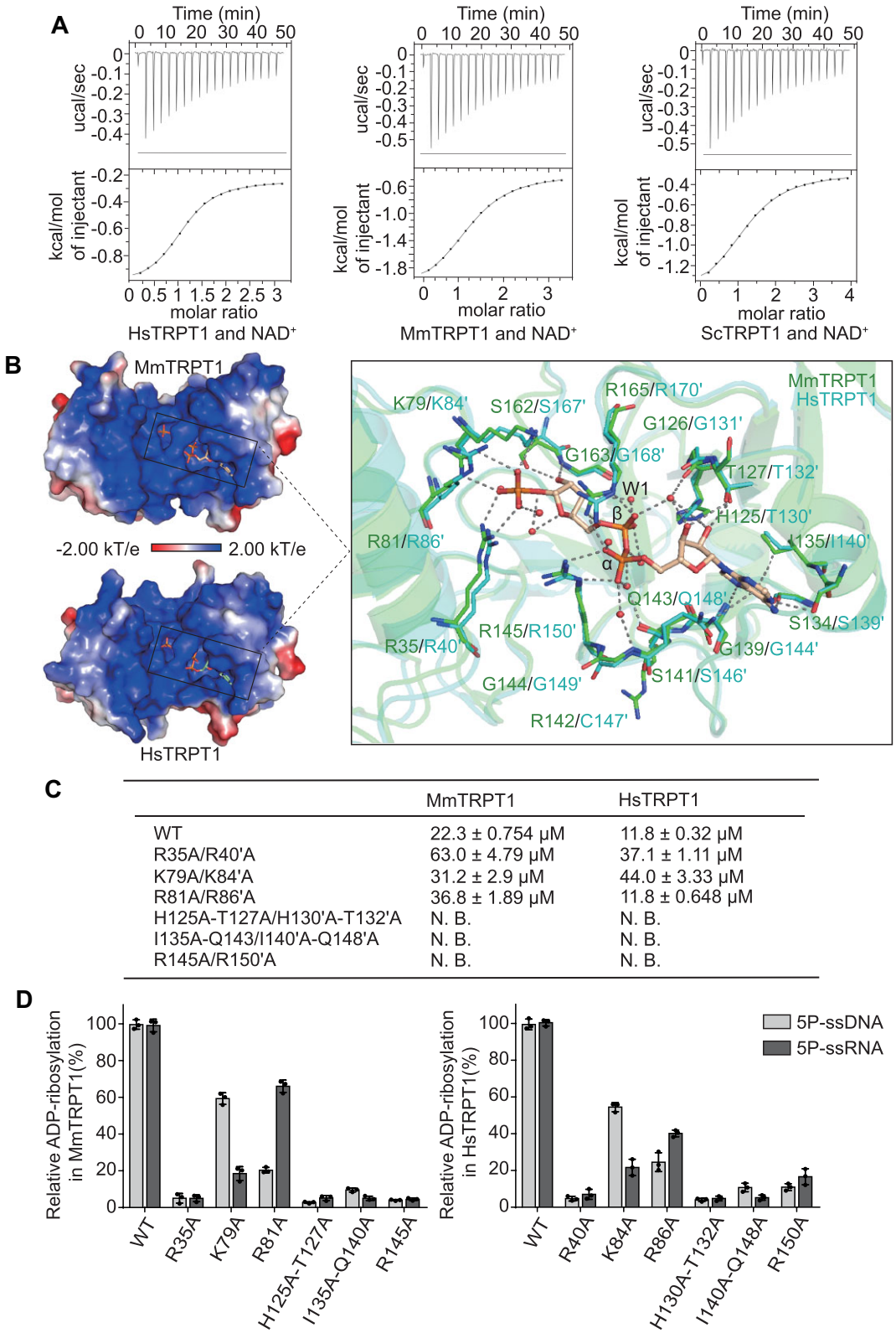

	MmTRPT1	HsTRPT1
WT	22.3 ± 0.754 μM	11.8 ± 0.32 μM
R35A/R40'A	63.0 ± 4.79 μM	37.1 ± 1.11 μM
K79A/K84'A	31.2 ± 2.9 μM	44.0 ± 3.33 μM
R81A/R86'A	36.8 ± 1.89 μM	11.8 ± 0.648 μM
H125A-T127A/H130'A-T132'A	N. B.	N. B.
I135A-Q143/I140'A-Q148'A	N. B.	N. B.
R145A/R150'A	N. B.	N. B.

Figure 2. Structural analysis of the NAD^+-binding pocket in HsTRPT1 and MmTRPT1. (**A**) ITC titrations of NAD^+ with wild-type HsTRPT1, MmTRPT1 and ScTRPT1. (**B**) Electrostatic potential map of the NAD^+-binding pocket (left panel) and NAD^+ binding mode (right panel) in HsTRPT1/MmTRPT1. The NAD^+-binding pocket is in the zoomed-in region. The NAD^+-binding residues are rendered as a cyan stick and green stick in HsTRPT1 and MmTRPT1, respectively. The ADPRp ligand is depicted as a stick and the water molecule as a red sphere. The hydrogen bonds are shown as dashed lines. (**C**) The binding affinities of NAD^+ for the indicated alanine mutants in HsTRPT1 and MmTRPT1. The K_d value was the average of three independent experiments. WT, wild type; N. B., non-bound. (**D**) The ADP-ribosylation activities of the indicated alanine mutants in HsTRPT1 and MmTRPT1 toward ssDNA and ssRNA with a 5′-PO_4 end. The enzymatic activity of each indicated mutant is normalized to that of wild-type TRPT1. Data are represented as the mean ± standard deviation (SD) as indicated from three independent experiments.

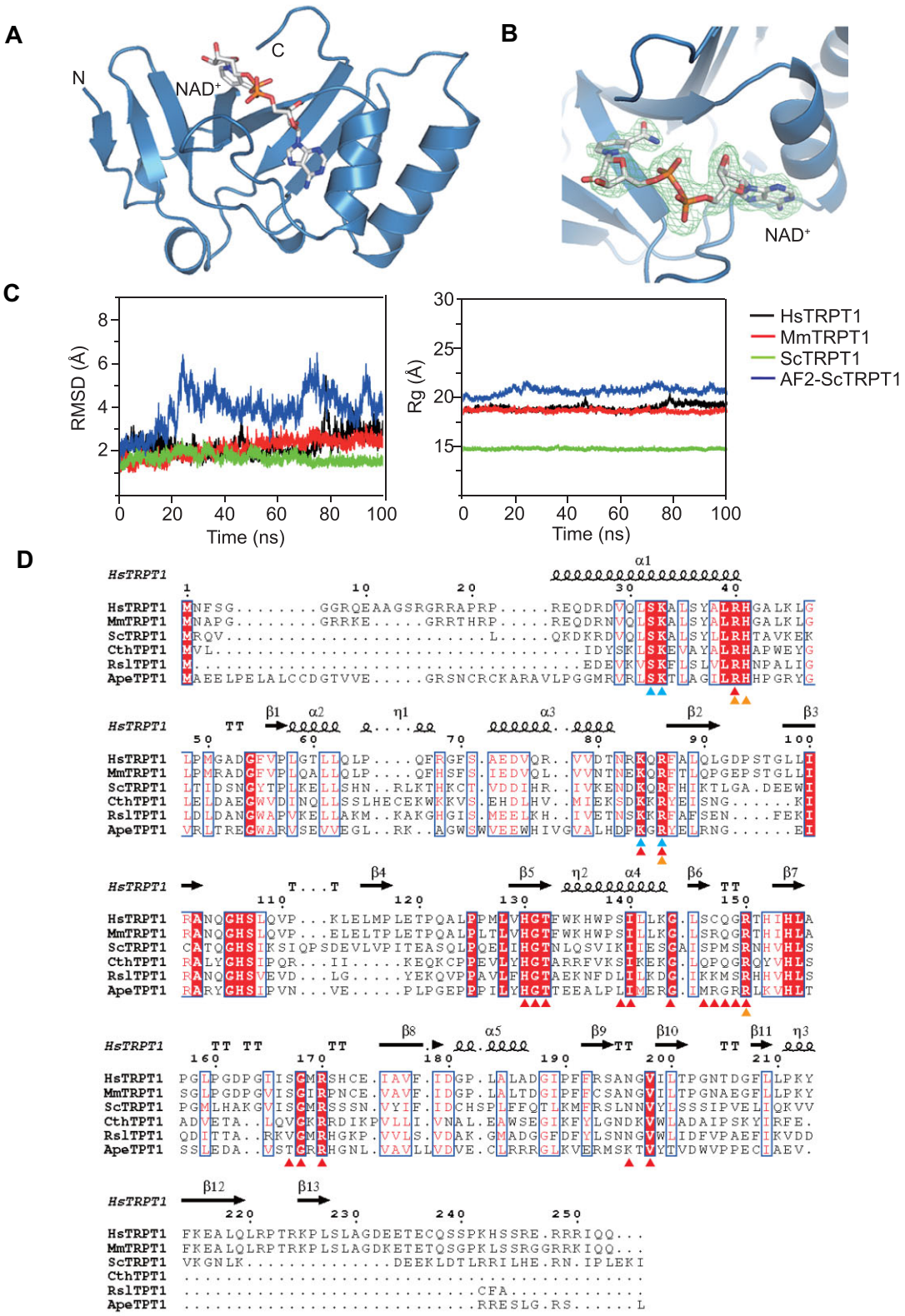

Figure 3. The intrinsic flexibility of TRPT1 from *S. cerevisiae* yielding the ScTRPT1$^{\text{NAD lobe}}$–NAD$^+$ complex. (**A**) Cartoon representation of the crystal structure of the ScTRPT1$^{\text{NAD lobe}}$–NAD$^+$ complex. The ScTRPT1$^{\text{NAD lobe}}$ is depicted as sky blue and the NAD$^+$ is depicted as a gray stick. (**B**) The 2*Fo*–*Fc* omit map of the NAD$^+$ contoured at 0.5 σ. (**C**) The RMSD values (left panel) and radius of gyration (Rg) values (right panel) of ScTRPT1$^{\text{NAD lobe}}$, AF2_ScTRPT1, MmTRPT1 and HsTRPT1. (**D**) Structure-based sequence alignment of TRPT1 homologs was generated via T-Coffee (41) and the results were displayed using ESPript3.0 (42). The secondary structural elements are labeled above the sequence. α, α-helix; β, β-sheet; η, 3_{10}-helix. The NAD$^+$- and nucleic acid-binding residues are marked in red and blue triangles, respectively. The catalytic residues essential for RNA 2′-phosphotransferase activity are shown as orange triangles. TRPT1 homologs from: *Homo sapiens* (HsTRPT1), *Mus musculus* (MmTRPT1), *Saccharomyces cerevisiae* (ScTRPT1), *Clostridium thermocellum* (CthTPT1), *Runella slithyformis* (RslTPT1) and *Aeropyrum pernix* (ApeTPT1).

NAD^+ lobes of TRPT1s. The presence of NAD^+, rather than ADPRp, and the degraded ScTRPT1 fragment in the crystal structure may be attributed to the linker loop connecting the RNA lobe and NAD^+ lobe in ScTRPT1, which is longer and more unstable than the corresponding loop in MmTRPT1 and HsTRPT1 (based on the Alphafold 2 model, named AF2_ScTRPT1), directly resulting in ScTRPT1 degradation. Indeed, we also observed ScTRPT1 degradation during protein storage and crystallization, and the macromolecular weight of the degraded fragment is consistent with the peptide chain length observed in the crystal structure, which is also confirmed by mass spectrometry analysis (data not shown).

In line with these observations, MD simulations of $ScTRPT1^{NAD\ lobe}$, AF2_ScTRPT1, MmTRPT1 and HsTRPT1 revealed that the RMSD value of $ScTRPT1^{NAD\ lobe}$ is lower than that of the other models, whereas the RMSD value of AF2_ScTRPT1 is highest among these structures, revealing the stable conformation of $ScTRPT1^{NAD\ lobe}$ and the flexible conformation of full-length ScTRPT1 (Figure 3C). Moreover, the radius of gyration (Rg) value for the $ScTRPT1^{NAD\ lobe}$ is found to be the smallest and is relatively stable throughout the simulation process (Figure 3C). In comparison, AF2_ScTRPT1 is loosely folded, indicating that the full-length ScTRPT1 has the largest degree of flexibility during simulation (Figure 3C). Taken together, all these results revealed the intrinsic flexibility of the full-length ScTRPT1, which is most probably provoked by the linker loop in ScTRPT1, contributing to ScTRPT1 degradation and NAD^+ integrity during crystallization. Thus, we propose that the intrinsic flexibility of ScTRPT1 may be associated with the low nucleic acid ADP-ribosylation activity. Indeed, the nucleic acid ADP-ribosylation activity of freshly prepared full-length ScTRPT1 protein is obviously higher than that of ScTRPT1 stored for a longer time (Figure 1A; Supplementary Figure S5B).

NAD^+ recognition in ScTRPT1

Consistent with MmTRPT1 and HsTRPT1, the shallow NAD^+-binding pocket occurs on the surface of the NAD^+ lobe (Figure 4A). The adenine ring is clamped by the Ile127–Met136 pair, corresponding to the Ile135–Gln143/Ile140′–Gln148′ pair in MmTRPT1/HsTRPT1. Similar to hydrogen bond contacts with adenine in MmTRPT1 and HsTRPT1, several hydrogen bonds are also observed between the adenine and its surrounding residues (Figure 4B). In detail, Ser134 (corresponding to Ser141/Ser146′ in MmTRPT1/HsTRPT1) forms a hydrogen bond with adenine-N7, Ala132 (corresponding to Gly139/Gly144′ in MmTRPT1/HsTRPT1) and Ser130 form hydrogen bonds with adenine-N6. The adenosine ribose 2′-OH forms bidentate hydrogen bonds with His117 (corresponding to His125/His130′ in MmTRPT1/HsTRPT1) and Thr119 (corresponding to Thr127/Thr132′ in MmTRPT1/HsTRPT1) from the conserved HGT motif. In addition, a water-mediated hydrogen bond network is formed between the adenosine ribose 3′-OH, β-phosphate and Gly118 (corresponding to Gly126/Gly131′ in MmTRPT1/HsTRPT1) of the HGT motif. Another water-mediated hydrogen bond network is also observed between α-phosphate, β-phosphate, Ser137, Arg138, His142, the distal ribose 2′-OH and 3′-OH. The nicotinamide moiety is sandwiched by the Met157–Val187 pair, corresponding to the Asn191–Val193/Asn196′–Val198′ pair in MmTRPT1/HsTRPT1. The nicotinamide forms hydrogen bonds with His117 and Gly118. Together, the adenine ring, adenosine ribose, diphosphate and nicotinamide are well stabilized by the surrounding residues via an extensive hydrogen bond network in ScTRPT1, and the binding modes for the adenine ring and adenosine ribose are conserved in both MmTRPT1 and HsTRPT1. Similarly, the ScTRPT1 mutants H117A–T119A, I127A–M136A and R138A lacked the binding activity to NAD^+, as well as the enzymatic activity on ssRNA and ssDNA ADP-ribosylation (Figure 4C, D; see also Supplementary Figures S5B and S6), demonstrating the conservation of NAD^+ binding to TRPT1s.

The conserved His–Thr pair from the HGT motif involved in the binding of the adenosine ribose moiety is found in all TRPT1 enzymes, diphtheria toxin-like bacterial ARTs and several mammalian PARPs, namely hPARP3, -7, -10, -11, -12, -14 and -15 (18,27,31,32). Additionally, the essential Ile135–Gln143/Ile140′–Gln148′ pair sandwiching the adenine ring is relatively conserved in the TRPT1 family members, and is replaced by the Ile129–Met136 pair in ScTRPT1 (Figure 3D). Thus, we suggest that the interactions with both the adenine ring and adenosine ribose serve as an important entrance for NAD^+ binding to TRPT1s, since these interactions do not require structural rearrangements in TRPT1s, they are crucial for both NAD^+ binding and catalysis, and they are conserved among TRPT1 homologs.

The dynamic recognition of NAD^+ in TRPT1s

The structural comparison of MmTRPT1/HsTRPT1 in a product-mimetic complex with ADPRp and of $ScTRPT1^{NAD\ lobe}$ in a complex with NAD^+ substrate provides useful insights into the mechanism of NAD^+ binding during the catalytic process. The ADP-ribose moiety shares an almost identical conformation with both ADPRp and NAD^+, whereas the disposition of the nicotinamide moiety connecting to the distal ribose in the ScTRPT1–NAD^+ complex varies greatly compared with 1″-PO_4 linked to the distal ribose in MmTRPT1/HsTRPT1 (Figure 5A). In the TRPT1–ADPRp complex, Ser162/Ser167′ and Gly163/Gly168′ form hydrogen bonds with the distal ribose 2″-OH, and Arg35/Arg40′, Lys79/Lys84′ and Arg81/Arg86′ stabilize the 1″-PO_4 in MmTRPT1/HsTRPT1 (Figure 2B). However, the corresponding residues Ser155 and Gly156 are absent in the structure of the $ScTRPT1^{NAD\ lobe}$–NAD^+ complex, and no electron density is observed for Arg23, Lys69 and Arg71 (corresponding to Arg35/Arg40′, Lys79/Lys84′ and Arg81/Arg86′ in MmTRPT1/HsTRPT1) owing to the RNA lobe degradation in ScTRPT1. The nicotinamide moiety rotated ∼100° clockwise compared with 1″-PO_4 in MmTRPT1/HsTRPT1, forming hydrogen bonds with His117 and Gly118 from the conserved HGT motif in ScTRPT1 (corresponding to His125/His130′ and

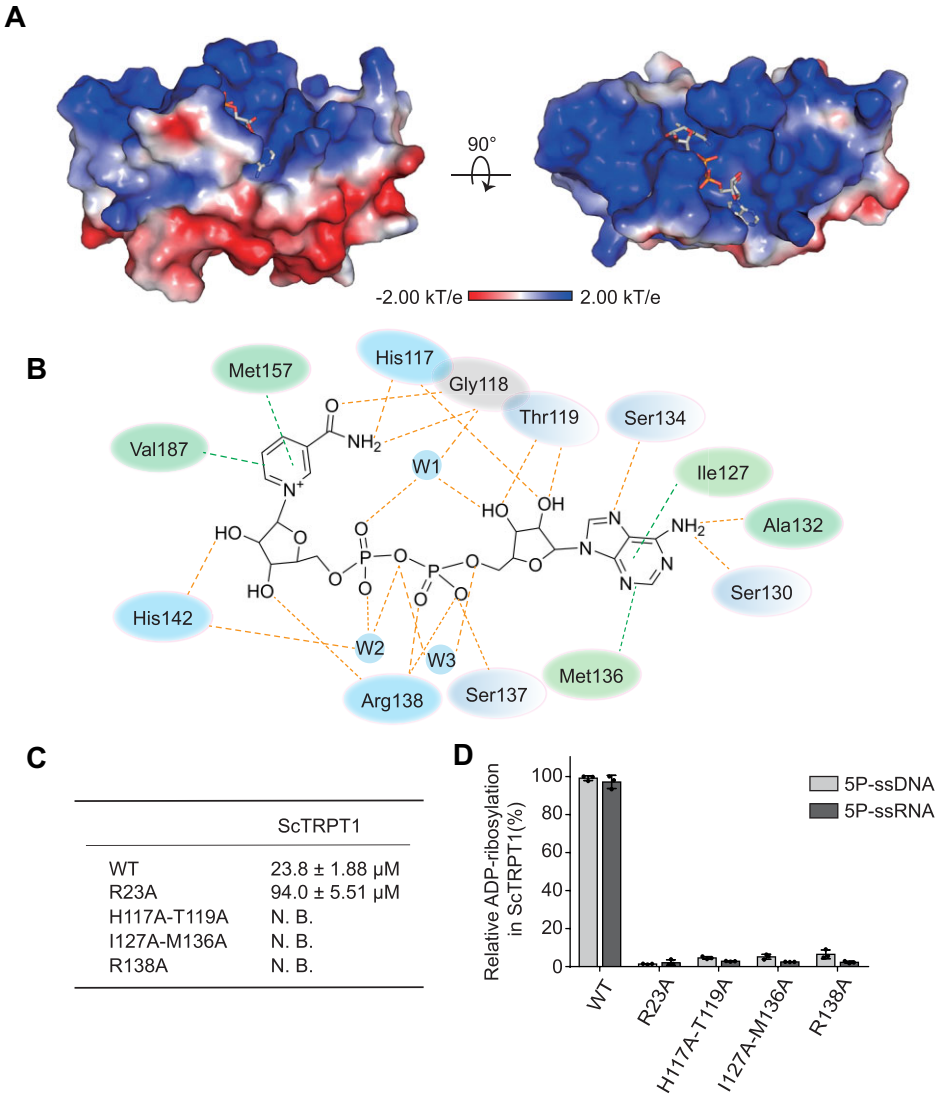

	ScTRPT1
WT	23.8 ± 1.88 μM
R23A	94.0 ± 5.51 μM
H117A-T119A	N. B.
I127A-M136A	N. B.
R138A	N. B.

Figure 4. NAD^+ binding mode in the $ScTRPT1^{NAD\ lobe}$. (**A**) Surface electrostatic model of the NAD^+-binding cavity in the $ScTRPT1^{NAD\ lobe}$. The right view is rotated 90° around the horizontal axis relative to the left view. (**B**) Two-dimensional ligand interaction mode between ScTRPT1 and NAD^+. The hydrogen bonds are depicted as orange dashed lines, and the π-stacking interactions are depicted as green dashed lines. W1, W2 and W3 represent water molecules 1, 2 and 3, respectively. (**C**) The binding affinities of NAD^+ for the indicated alanine mutants in ScTRPT1. The K_d value was the average of three independent experiments. WT, wild type; N. B., non bound. (**D**) The ADP-ribosylation activities of the indicated alanine mutants in ScTRPT1 toward ssDNA and ssRNA with a 5′-PO_4 end. The activity of each indicated mutant is normalized to the activity of the wild-type TRPT1. Data are represented as the mean ± SD as indicated from three independent experiments.

Gly126/Gly131′ in MmTRPT1/HsTRPT1, Figures 5A and 4B).

Given that ADPRp is a mimetic product and NAD^+ is a natural substrate, we superimposed the structures of MmTRPT1, HsTRPT1, AF2_ScTRPT1 and $ScTRPT1^{NAD\ lobe}$, and found that the nicotinamide moiety from the structure of $ScTRPT1^{NAD\ lobe}$ generates severe steric hindrance with serine and glycine from the donor loop (Ser162/Ser167′/Ser155″ and Gly163/Gly168′/Gly156″, where ″ indicates the parallel residue in ScTRPT1) (Figure 5A). In addition, structural superimpositions between the TRPT1–ADPRp complexes and their AlphaFold2 models (as apo-TRPT1s) reveal that the most significant structural variation in the active groove is the donor loop (Figure 5B). In the apo-TRPT1s model, the donor loop is in an outward-facing conformation, whereas in the ADPRp-bound TRPT1s, it exhibits an inward-facing conformation, enabling the residues (Ser162/Ser167′ and Gly163/Gly168′) from this loop to bind and accommodate the distal ribose (Figures 2B and 5B). Importantly, the side chain of Ser162/Ser167′ rotated ∼180°, and the hydroxyl group moved ∼8 Å towards the ADPRp-binding site. Meanwhile, Gly163/Gly168′ shifted ∼2.9–4.1 Å towards the ADPRp-binding site (Figure 5B). Consequently, a hydrogen bond network is formed between the distal ribose moiety of ADPRp, Ser162/Ser167′ and Gly163/Gly168′ (Figure 2B). These interactions are responsible for the binding of the mimetic product ADPRp in the NAD^+ lobe.

To provide more insights into the dynamics and structural properties of the TRPT1–NAD^+ (or ADPRp)

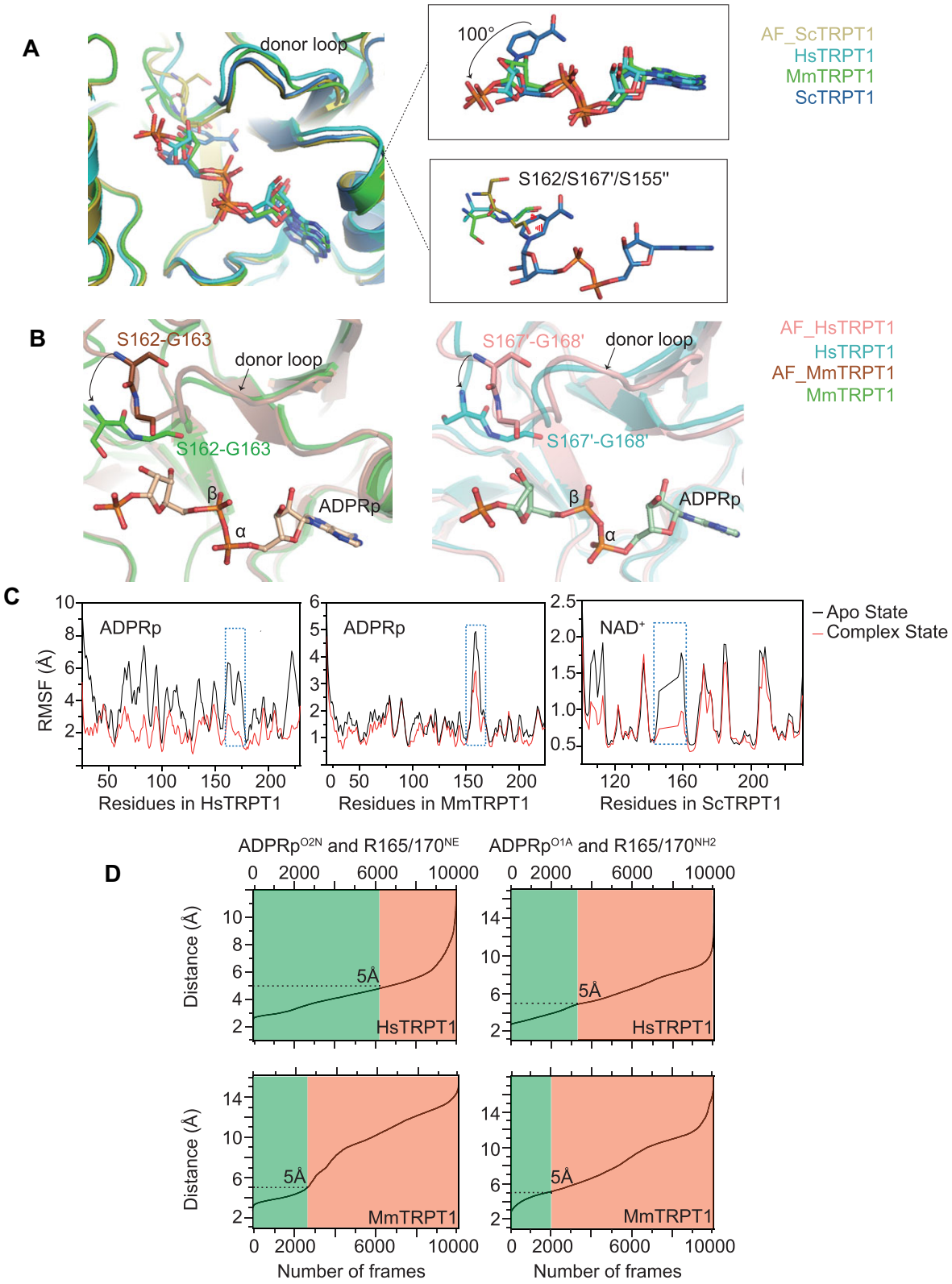

Figure 5. NAD^+ recognition dynamics in TRPT1s. (**A**) Structural superimpositions highlight the flipping of the nicotinamide moiety in the active site. The arrow represents the conformation change of NAD^+ compared with ADPRp. The steric hindrance is presented by red lines. (**B**) Structural comparisons of TRPT1s with their AlphaFold2 models. Left panel, MmTRPT1; right panel, HsTRPT1. (**C**) Comparison of RMSF values between the apo state and ligand binding state. From left to right: HsTRPT1, MmTRPT1 and ScTRPT1. The donor loop (β7–β8 loop) is framed by a blue dashed line. (**D**) The distance of ADPRp and R165/170 was monitored during MD simulation and plotted in the diagram, $ADPR^{O2N}$ and $R165/170^{NE}$ (left panel), $ADPRp^{O1A}$ and $R165/170^{NH2}$ (right panel).

complex in solution, MD simulations were carried out for TRPT1s and their respective ligands. Compared with apo-TRPT1s, the RMSF value of the donor loop was substantially reduced upon NAD^+ or ADPRp binding (Figure 5C). A previous study showed that the Arg139 in CthTPT1 (corresponding to Arg165/Arg170′/Arg158″) may function as a key to open the NAD^+ entry path by comparing the CthTPT1 and apo-ApeTPT1 structures (18). In the complex structure of MmTRPT1/HsTRPT1, the O2N and O1A atoms of ADPRp are hydrogen-bonded to the NE and NH2 atoms of Arg165/Arg170′, respectively (Figure 2B), which is adjacent to Ser162/Ser167′ and Gly163/Gly168′ of the donor loop. Thus, the interactions between ADPRp and Arg165/Arg170′ were monitored during MD simulation (Figure 5D). In ∼20–60% of the 10 001 frames with 100 ns simulation, Arg165/Arg170′ adopt a closed conformation in TRPT1s, in which the NE and NH2 of Arg165/Arg170′ are close to the O2N and O1A of ADPRp (the distance between them is <5 Å), facilitating the binding with ADPRp. In ∼40–80% of frames, Arg165/Arg170′ adopt open conformations in TRPT1s, in which the NE and NH2 of Arg165/Arg170′ are far away from ADPRp (the distance between them is >5 Å) and do not interact with ADPRp (Figure 5D). Combining the conformational changes of Ser162/Ser167′ and Gly163/Gly168′ in MmTRPT1/HsTRPT1 crystal structures (Figure 5B), these results revealed that the donor loop undergoes a significant conformational change upon NAD^+ binding, which is largely driven by the displacement of the conserved serine, glycine and arginine, making NAD^+ reside in a favorable orientation and facilitate the catalytic reaction.

Indeed, the mutations of serine, glycine or serine–glycine to tryptophan almost abolished the ADP-ribosylation activity of TRPT1s (Supplementary Figure S5C), suggesting that the flexibility of serine and glycine is important for placing the NAD^+ in the correct orientation during the catalytic process, and the bulky aromatic side chain of tryptophan may impede the favorable conformation of NAD^+, leading to abortion of the catalytic reaction. The high flexibility of the donor loop indicates that this loop may function as a switch loop to facilitate the turnover of substrate and product. The Ser–Gly–X–Arg sequence, termed the 'SGR' motif, from the dynamic donor loop is highly conserved among eukaryotic TRPT1 members (Figure 3D; Supplementary Figure S7), indicating that eukaryotic TRPT1s could utilize the common mechanism for NAD^+ substrate recognition and catalysis. In comparison, the SGR motif is substituted by other amino acids and forms a small α-helix in bacteria and archaea (Figure 3D; Supplementary Figures S3 and S7), generating significant structural difference in the catalytic pocket among TRPT1 family members, which may be associated with NAD^+ binding diversity.

The RNA binding mode in MmTRPT1/HsTRPT1

Nucleic acids work as another substrate of TRPT1s; the ITC assays revealed that the K_d between ssDNA substrate and ScTRPT1 is 11.6 ± 1.59 μM with 1:1 stoichiometric binding, and the K_d values are 1.19 ± 0.067 μM and 0.39 ± 0.001 μM for ssDNA bound to MmTRPT1 and HsTRPT1 respectively, indicating the higher binding affinity of nucleic acid for mammalian TRPT1 and lower affinity of nucleic acid for ScTRPT1 (Figure 6A; Supplementary Table S4B).

The electrostatic potential surface represents a positively charged clamp-like pocket in the RNA lobe of MmTRPT1/HsTRPT1 (Figure 6B), mainly composed of Ser27/Ser32′, Lys28/Lys33′, Lys79/Lys84′ and Arg81/Arg86′ (equivalent to Ser15″, Lys16″, Lys69″ and Arg71″ in ScTRPT1), which may be important for nucleic acid substrate binding (Figure 6B). Thus, a series of mutational experiments were performed in MmTRPT1 and HsTRPT1 to measure the enzymatic activities on nucleic acid ADP-ribosylation. All MmTRPT1 mutants (S27A, K28A, S27A–K28A, K79A and R81A) exhibit reduced ADP-ribosylation activity (Figure 6C; Supplementary Figure S5A), while these mutants have binding affinities for NAD^+ similar to that of wild-type MmTRPT1 (Supplementary Figure S4A; Supplementary Table S4A). In particular, the double mutant S27A–K28A retained ∼17% and 8% enzymatic activity towards ssDNA and ssRNA, respectively (Figure 6C; Supplementary Figure S5A), indicating that the Ser27–Lys28 pair plays an important role in the binding with nucleic acid substrate. Additionally, the mutant K79A retained 60% and 21% enzymatic activity towards ssDNA and ssRNA, respectively, while the mutant R81A retained 19.6% and 61% enzymatic activity towards ssDNA and ssRNA, respectively (Figure 6C; Supplementary Figure S5A), suggesting that the residues Lys79 and Arg81 play key roles in the preferred binding of ssRNA and ssDNA, respectively, which is in good agreement with the general feature that arginine mainly binds to DNA, and lysine prefers binding to RNA (33–35).

Similar results are observed among the corresponding mutants in HsTRPT1 (Figure 6C; Supplementary Figures S4B and S5A; Supplementary Table S4A), revealing that the Ser27–Lys28/Ser32′–Lys33′ pair, Lys79/Lys84′ and Arg81/Arg86′ play significant roles in the nucleic acid substrate binding of MmTRPT1/HsTRPT1. We also suggest that the functional redundancy in nucleic acid-binding residues provides structural flexibility to accommodate different types of nucleic acid substrate. Sequence alignment revealed that these nucleic acid-binding residues are highly conserved in TRPT1-family proteins (Figure 3D), indicating that TRPT1s employ a common nucleic acid binding mode as observed in MmTRPT1/HsTRPT1.

TRPT1s employ diverse residues towards RNA 2′-phosphotransferase and ART activities

Previous studies have reported that both MmTRPT1 and HsTRPT1 exhibit RNA 2′-phosphotransferase activity *in vitro* and are able to genetically complement the lethal *ScTrpt1*Δ knockout in *S. cerevisiae* (13,31). They suggest that the mutants of essential residues for tRNA 2′-phosphotransferase activity in MmTRPT1/HsTRPT1 fail to complement the lethal *ScTrpt1*Δ knockout in *S. cerevisiae*. Thus we used the lethal phenotype generated in the complementation assay in yeast to characterize the residues contributing to RNA 2′-phosphotransferase activity in MmTRPT1/HsTRPT1. The MmTRPT1/HsTRPT1-Ala alleles on modified p414 plasmid were tested for the complementation of *ScTrpt1*Δ in *S. cerevisiae* by plasmid shuffling (18,27). The TRPT1s mutants I135A–

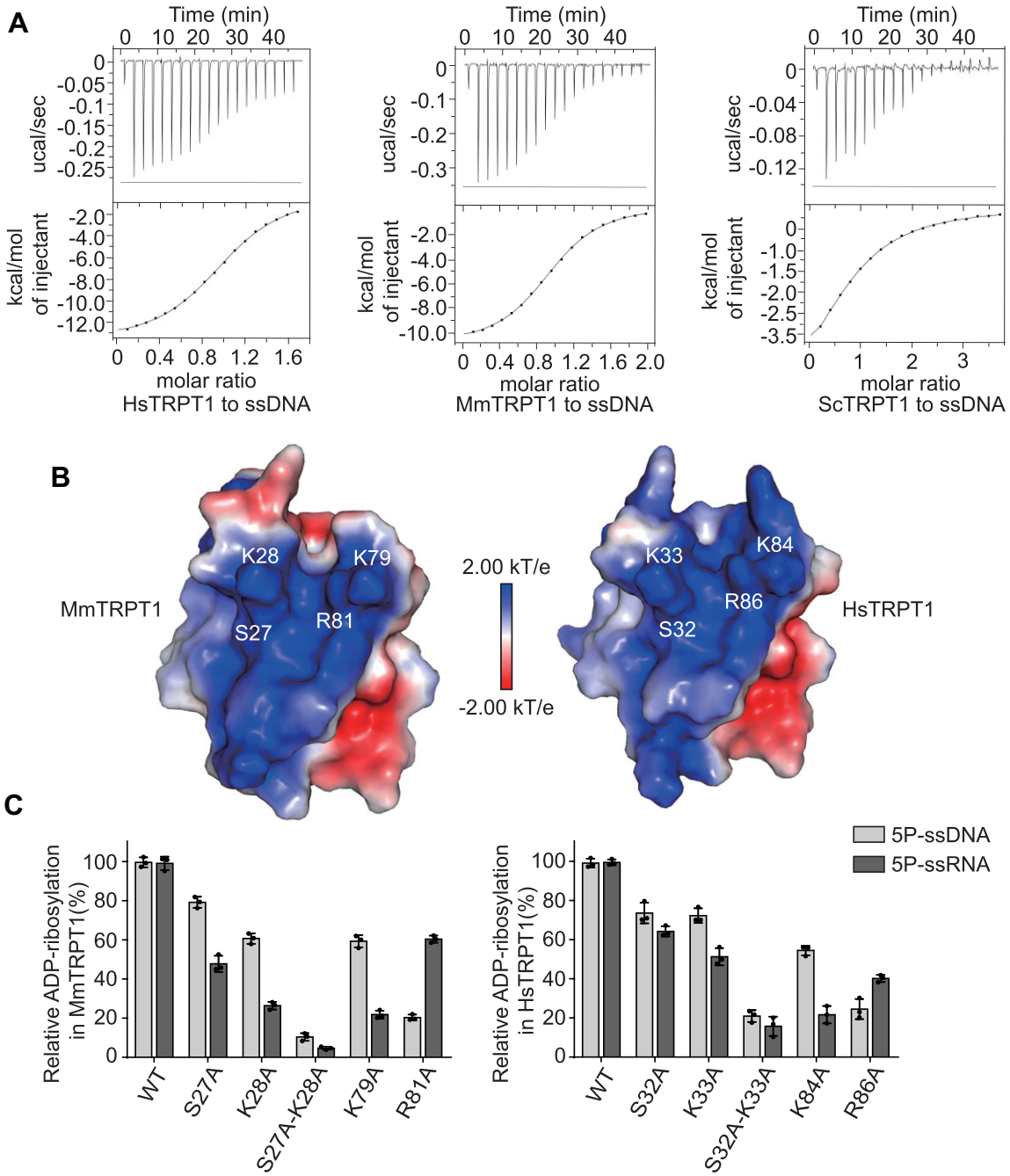

Figure 6. RNA binding mode in eukaryotic TRPT1s. (**A**) The ITC titrations of ssDNA with wild-type HsTRPT1, MmTRPT1 and ScTRPT1. (**B**) Surface electrostatic model of the RNA lobe in MmTRPT1 (left panel) and HsTRPT1 (right panel). The nucleic acid-binding residues are highlighted in white. (**C**) The nucleic acid ADP-ribosylation activities of the indicated alanine mutants in HsTRPT1 and MmTRPT1. The enzymatic activity of each indicated mutant is normalized to that of wild-type TRPT1. Data are represented as the mean ± SD as indicated from three independent experiments.

Q143A/I140′A–Q148′A, H125A–T127A/H130′A–T132′A and N191A–V193A/N196′A–V198′A failed to give rise to 5-FOA-resistant colonies after incubation for 8 days, and thus were deemed lethal *in vivo* (Figure 7; Supplementary Figure S8), indicating that interactions with the adenine (Ile135–Gln143/Ile140′–Gln148′), adenosine ribose (His125–Thr127/His130′–Thr132′) and nicotinamide (Asn191–Val193/Asn196′–Val198′) moieties of NAD^+ are essential for MmTRPT1/HsTRPT1 RNA 2′-phosphotransferase activity *in vivo*, which is in good agreement with the previous study on *Runella slithyformis* TPT1 (RslTPT1) (27). Similarly, the interactions with the adenine and adenosine ribose are essential for nucleic acid ADP-ribosylation activity (Figure 2D; Supplementary Figure S5A), while the interaction with the nicotinamide moiety is not necessary for nucleic acid ADP-ribosylation in MmTRPT1/HsTRPT1, since the mutants N191A–V193A/N196′A–V198′A retain partial enzymatic

Contact	TRPT1 mutant	*ScTrpt1*Δ TRPT1 complementation
Nucleic acid binding	S27A/S32'A	viable
	K28A/K33'A	viable
	S27A-K28A/S32'A-K33'A	lethal
	K79A/K84'A	viable
	R81A/R86'A	lethal
	R35A/R40'A	lethal
	H36A/H41'A	lethal
	R145A/R150'A	lethal
NAD⁺ binding	R35A-R145A/R40'A-R150'A	lethal
	H125A-T127A/H130'A-T132'A	lethal
	I135A-Q143A/I140'A-Q148'A	lethal
	R145A-R165A/R150'A-R170'A	lethal
	N191A-V193A/N196'A-V198'A	lethal

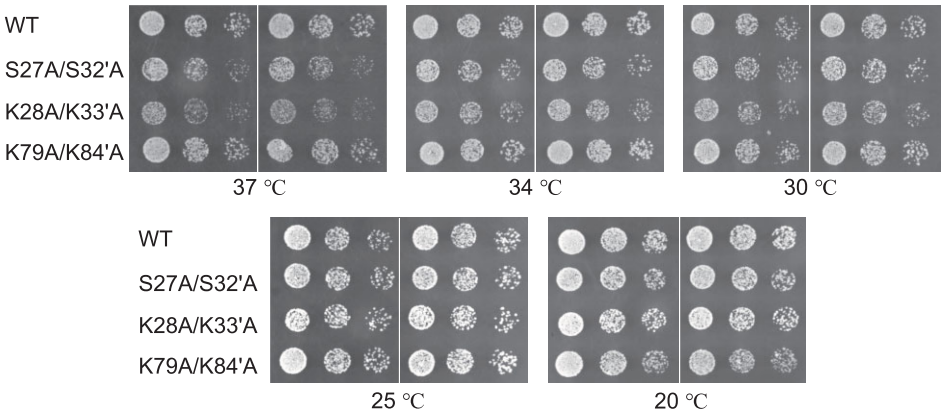

Figure 7. TRPT1s adopt diverse residues towards 2′-phosphotransferase and ART activities. The RNA 2′-phosphotransferase activity of the indicated HsTRPT1/MmTRPT1 alanine mutants in *ScTrpt1*Δ complementation was carried out by plasmid shuffling as indicated in the Materials and Methods. The NAD^+- and nucleic acid-binding residues are denoted as red and blue circles, respectively. The catalytic residues essential for RNA 2′-phosphotransferase activity are shown as orange circles. The results are summarized in the top panel. Serial dilutions of the viable *S. cerevisiaeTrpt1*Δ strains expressing wild-type (WT) MmTRPT1 (left) or HsTRPT1 (right) and the indicated mutants were spot-tested for growth on YPD agar at the temperature specified (bottom panel).

activities on nucleic acid ADP-ribosylation (Supplementary Figure S5A).

Furthermore, we found that the mutants S27A–K28A/S32′A–K33′A were lethal when tested for *ScTrpt1*Δ complementation, while the mutants K79A/K84′A grew as well as wild-type TRPT1s (Figure 7), revealing that the Ser27–Lys28/Ser32′–Lys33′ pair, rather than Lys79/Lys84′, is essential for RNA substrate binding in the RNA 2′-phosphotransferase activity *in vivo*. Considering the functional redundancy of the Ser27–Lys28/Ser32′–Lys33′ pair, Lys79/Lys84′ and Arg81/Arg86′ in nucleic acid substrate binding during the process of nucleic acid ADP-ribosylation, it suggests that the nucleic acid substrate-binding residues may be different towards 2′-phosphotransferase and ART, probably due to the conformational diversity of different types of nucleic acid substrate used in different catalytic reactions.

The catalytic residues for 2′-phosphotransferase activity consist of Arg23, His24, Arg71 and Arg138 in ScTRPT1, equivalent to Arg35/Arg40′, His36/His41′, Arg81/Arg86′ and Arg145/Arg150′ in MmTRPT1/HsTRPT1 (31). Therefore, all catalytic mutants were unable to grow on agar medium containing 5-FOA, revealing their catalytic roles in 2′-phosphotransferase activity *in vivo* (Figure 7). Similarly, the mutants R35A/R40′A, H36A/H41′A and R145A/R150′A completely lacked nucleic acid ADP-ribosylation activity (Figure 2D; Supplementary Figure S5A). Considering that Arg35/Arg40′ and His36/His41′ are not required for NAD^+ binding (Figure 2B, C), this suggests that Arg35/Arg40′ and His36/His41′ play essential catalytic roles in the nucleic acid ADP-ribosylation activity. However, the mutants R81A/R86′A retained ∼20% and 50% ADP-ribosylation activity towards ssDNA and ssRNA, respectively (Figure 6C; Supplementary Figure S5A), indicating that Arg81/Arg86′, the essential catalytic residue in 2′-phosphotransferase, functions as a redundant nucleic acid-binding residue, rather than a catalytic residue, in the catalytic processes of ART.

DISCUSSION

The tRNA 2′-phosphotransferase TRPT1 is an essential enzyme of the fungal tRNA splicing pathway that catalyzes the transfer of RNA internal 2′-phosphate to NAD^+ via a two-step reaction (14,16,17). TRPT1 homologs are widespread across different taxa, many of which do

not require RNA 2′-phosphotransferase activity *in vivo*, suggesting that TRPT1 might catalyze other reactions, rather than only RNA 2′-phosphate removal (18). Recent studies have shown that TRPT1 homologs from bacteria, fungi and archaea possess ADP-ribosylation activity towards nucleic acids, raising the prospect that nucleic acid ADP-ribosylation is a conserved enzyme activity of TRPT1 family members across all domains of life (1,9,11,13). However, the molecular mechanism of TRPT1-dependent nucleic acid ADP-ribosylation has remained unclear. In this study, we have determined the crystal structures of HsTRPT1, MmTRPT1 and ScTRPT1 with their NAD^+ substrates. Notably, the crystal structures of HsTRPT1 and MmTRPT1 contain one ADPRp molecule, while the degraded fragment of the ScTRPT1 structure contains one NAD^+ molecule. In our opinion, the ADPRp molecule in crystal structures of HsTRPT1 and MmTRPT1 would be generated during the co-crystallization of HsTRPT1/MmTRPT1 with NAD^+. As the N-terminal RNA lobe of TRPT1s is involved in nucleic acid binding, endogenous *E. coli* nucleic acid (probably 2′-PO_4 branched RNA) can be co-purified with recombinant TRPT1s. During the crystal growth stage, the recombinant TRPT1 proteins are able to catalyze these 2′-PO_4 branched RNA substrates to form ADP-ribose-1″,2″-cyclic phosphates, which are in turn hydrolyzed *in situ* to ADPRp. Additionally, the ligand diversity in the structure of ScTRPT1 could also provide a strong support for our hypothesis. Owing to the degradation of the N-terminal RNA lobe in ScTRPT1, ScTRPT1 cannot catalyze 2′-PO_4 branched RNA substrates to generate ADPRp, thus leading to the original NAD^+ substrate, rather than the ADPRp by-product, observed in the crystal structure of ScTRPT1.

Next, we investigated the detailed structural basis for NAD^+ recognition, dynamic and biochemical analyses of these TRPT1s. Our results highlight that: (i) all members of TRPT1s share a conserved core fold comprising an RNA lobe and an NAD^+ lobe, except for the differences in length and conformation of the linker loop and donor loop, whereby the linker loop may lead to the flexibility of the overall structure, and the donor loop could be associated with the NAD^+ recognition and catalysis; (ii) the donor loop with high flexibility mainly imparted by the conserved SGR motif may serve as a switch loop to facilitate the turnover of substrate and product; (iii) several residues located on the RNA lobe contribute to nucleic acid binding, and the functional redundancy of nucleic acid-binding residues provides structural flexibility to accommodate alternative nucleic acid substrates, and the TRPT1s may bind the nucleic acid substrates using the common mode; and (iv) TRPT1s adopt different catalytic residues and nucleic acid-binding residues towards RNA 2′-phosphotransferase and ART activities.

Additionally, as our results revealed that ScTRPT1 possesses intrinsic flexibility and low nucleic acid ADP-ribosylation activity, we suggest that the significant difference in nucleic acid ADP-ribosylation activity among HsTRPT1/MmTRPT1 and ScTRPT1 may be attributed to the intrinsic flexibility of ScTRPT1 and the low binding affinity of ScTRPT1 for nucleic acids (Figure 6A). However, we cannot rule out the possibility that the activity difference in nucleic acid ADP-ribosylation could also be attributed to the discrepancy in the main reaction catalyzed by TRPT1s from different species.

PARP family members, including PARP1–PARP3, PARP10, PARP11 and PARP15, are able to ADP-ribosylate protein and nucleic acid, while the PARP-like protein TRPT1 is only able to ADP-ribosylate nucleic acid, indicating that TRPT1 is different from PARP family members. Structural comparison revealed that the TRPT1 NAD^+ lobe is more compact than the canonical PARP catalytic domain (ADP-ribosyltransferase domain, ART domain) (Supplementary Figure S9A). The characteristic donor and acceptor loops in the ART domain (12) are also observed in TRPT1s, while the two loops in TRPT1s are different from those of PARPs in orientation, length and rigidity, all of which are potentially associated with their diverse enzymatic functions. The catalytic domain of PARP1–PARP5 contains a classical ART signature H-Y-E motif, and a variant H-Y-I/L motif is observed in the mono(ADP-ribosyl)ases PARP10, PARP11 and PARP15 (Supplementary Figure S9B). Specifically, the glutamate in the H-Y-E motif is replaced with residues Ile^{987}, Ile^{320} and Leu^{637} in PARP10, PARP11 and PARP15, respectively, correlating with their mono-ART activities (8,36,37). Structural comparisons revealed a variant H-H-V motif composed of His^{125}–His^{149}–Val^{193} in the NAD^+ lobe of MmTRPT1 (equivalent to His^{130}–His^{154}–Val^{198} and His^{117}–His^{142}–Val^{187} in HsTRPT1 and ScTRPT1, respectively), belonging to the H-H-h (hydrophobic) motif (Supplementary Figure S9B) (36,38). The first histidine in the H-H-V motif is conserved in the classical H-Y-E motif, and they play equivalent roles, contributing to the binding of both adenosine ribose and nicotinamide via hydrogen bonds. The glutamate in the H-Y-E motif plays an essential catalytic role in the poly(ADP-ribose) transferase activity, while the glutamate is replaced by valine in TRPT1s, only stabilizing the nicotinamide moiety. In addition, the tyrosine in the H-Y-E motif is involved in distal ribose stacking (12,36,39), while the corresponding residue in TRPT1 is histidine, which forms a hydrogen bond with the distal ribose. This suggests the significant diversities in NAD^+ incorporation pattern between TRPT1s and PARPs. Together, the variant H-H-V motif in TRPT1 is only involved in NAD^+ substrate binding, and does not possess a catalytic role compared with the classical H-Y-E motif, consequently enabling TRPT1 to perform mono-ART activity using a different mechanism compared with that of PARPs.

Our biochemical data revealed that TRPT1s can exclusively ADP-ribosylate 5′-phosphorylated nucleic acid substrates (Figure 1A), revealing the significance of the phosphate group from the substrate in the process of nucleic acid ADP-ribosylation, which is consistent with the previous studies (12,13,40). Combining these biochemical data, we hypothesize that TRPT1 catalyzes the ART reaction employing the substrate-assisted catalysis mechanism, in which the 5′-PO_4 from the nucleic acid substrate functions as the nucleophile to attack the distal ribose C1 carbon of NAD^+ and release the nicotinamide moiety of NAD^+,

leading to the covalent attachment of ADP-ribose to the 5′-PO_4 nucleic acid terminus.

It has been reported that nucleic acid ADP-ribosylation may play important roles in many biological processes, including epigenetics, DNA repair and replication (1,12,38,39), and Weixler *et al*. recently found that diverse cellular stressors can mediate nucleic acid ADP-ribosylation in mammalian cells (11), raising an interesting question of whether HsTRPT1 is associated with cancer cell survival and proliferation in some way. Thus we carried out pan-cancer *in silico* analysis of HsTRPT1 expression between normal and primary tumor tissues using the RNA sequencing data from the TCGA database. We found that HsTRPT1 is aberrantly up-regulated in many types of cancers, including cervical squamous cell carcinoma (CESC), uterine corpus endometrial carcinoma (UCEC), cholangiocarcinoma (CHOL) and bladder urothelial carcinoma (BLCA), compared with the paired non-cancerous tissues (Supplementary Figure S10A). Additionally, we examined genetic alternations of TRPT1 in diverse cancers using the cBIOportal database, and found that gene amplification is the main alteration type (Supplementary Figure S10B). In this study, we selected CESC for further analysis. Using the 'Histological subtype' module, we observed that five CESC subtypes encompassing adenosquamous, squamous cell, endocervical, mucinous and endometrioid are included in the pan-cancer *in silico* analysis. It is shown that TPRT1 is up-regulated in endocervical, endometrioid and mucinous subtypes (Supplementary Figure S10C). We further validated the high expression of TRPT1 in CESC cell lines HeLa and C-33A compared with that in normal human cervical epithelial cells, which are primary cervical epithelial cells isolated from the normal cervical tissue (Supplementary Figure S10D).

To explore whether TRPT1 is associated with CESC cell survival and proliferation, we knocked down HsTRPT1 in endocervical HeLa cells using two independent shRNAs, and employed the two shRNAs for the following experiments (Supplementary Figure S11A). The colony formation assays revealed that HsTRPT1 KD significantly reduced the colony-forming ability of HeLa cells (Supplementary Figure S11B, C). Meanwhile, the CCK-8 assays demonstrated that HsTRPT1 KD markedly compromised cell proliferation in HeLa cells (Supplementary Figure S11B, D). Notably, the HsTRPT1 re-expression restored the colony-forming capacity and cell proliferation in HeLa cells (Supplementary Figure S11B, C, D). These results showed that HsTRPT1 is able to promote endocervical HeLa cell survival and growth, indicating that mammalian TRPT1 may be associated with CESC cell survival and proliferation. Therefore, our results provide an interesting clue for the potential role of HsTRPT1 in mammalian cells.

DATA AVAILABILITY

The atomic coordinates and structure factors for the HsTRPT1–ADPRp, MmTRPT1–ADPRp and ScTRPT1–NAD^+ complexes have been deposited in the Protein Data Bank with the accession codes 7YW3, 7YW2 and 7YW4, respectively. Original images of gels and western blots are shown in Supplementary Figures S12 and S13.

SUPPLEMENTARY DATA

Supplementary Data are available at NAR Online.

ACKNOWLEDGEMENTS

We thank the Beamline BL19U1 staff at the Shanghai Synchrotron Radiation facility for the X-ray data collection.
Author contributions: X.L. designed and administrated the project. J.W., S.L., X.L. and J.G. performed the experiments. X.Y., J.W., Z.Y. and X.L. analyzed the data. H.Z. collected X-ray diffraction data. C.W., X.Y. and X.L. wrote the manuscript.

FUNDING

The National Natural Science Foundation of China [32171295 and 32071277]; Foundation of Hebei Educational Committee [ZD2020183]; the Natural Science Foundation of Hebei Province [C2022201025 and C2020201030]; Hebei Province Foundation for Returned Overseas Chinese Scholars [C20200303]; and the Interdisciplinary Research Program of Natural Science of Hebei University [DXK202006 and DXK202007].
Conflict of interest statement. None declared.

REFERENCES

1. Groslambert,J., Prokhorova,E. and Ahel,I. (2021) ADP-ribosylation of DNA and RNA. *DNA Repair (Amst.)*, **105**, 103144.
2. Barkauskaite,E., Jankevicius,G. and Ahel,I. (2015) Structures and mechanisms of enzymes employed in the synthesis and degradation of PARP-dependent protein ADP-ribosylation. *Mol. Cell*, **58**, 935–946.
3. Gibson,B.A. and Kraus,W.L. (2012) New insights into the molecular and cellular functions of poly(ADP-ribose) and PARPs. *Nat. Rev. Mol. Cell Biol.*, **13**, 411–424.
4. Martin-Hernandez,K., Rodriguez-Vargas,J.M., Schreiber,V. and Dantzer,F. (2017) Expanding functions of ADP-ribosylation in the maintenance of genome integrity. *Semin. Cell Dev. Biol.*, **63**, 92–101.
5. Palazzo,L., Mikoc,A. and Ahel,I. (2017) ADP-ribosylation: new facets of an ancient modification. *FEBS J.*, **284**, 2932–2946.
6. Hou,W.H., Chen,S.H. and Yu,X. (2019) Poly-ADP ribosylation in DNA damage response and cancer therapy. *Mutat. Res. Rev. Mutat. Res.*, **780**, 82–91.
7. Crawford,K., Bonfiglio,J.J., Mikoc,A., Matic,I. and Ahel,I. (2018) Specificity of reversible ADP-ribosylation and regulation of cellular processes. *Crit. Rev. Biochem. Mol. Biol.*, **53**, 64–82.
8. Vyas,S., Matic,I., Uchima,L., Rood,J., Zaja,R., Hay,R.T., Ahel,I. and Chang,P. (2014) Family-wide analysis of poly(ADP-ribose) polymerase activity. *Nat. Commun.*, **5**, 4426.
9. Munnur,D., Bartlett,E., Mikolcevic,P., Kirby,I.T., Rack,J.G.M., Mikoc,A., Cohen,M.S. and Ahel,I. (2019) Reversible ADP-ribosylation of RNA. *Nucleic Acids Res.*, **47**, 5658–5669.
10. Zarkovic,G., Belousova,E.A., Talhaoui,I., Saint-Pierre,C., Kutuzov,M.M., Matkarimov,B.T., Biard,D., Gasparutto,D., Lavrik,O.I. and Ishchenko,A.A. (2018) Characterization of DNA ADP-ribosyltransferase activities of PARP2 and PARP3: new insights into DNA ADP-ribosylation. *Nucleic Acids Res.*, **46**, 2417–2431.
11. Weixler,L., Feijs,K.L.H. and Zaja,R. (2022) ADP-ribosylation of RNA in mammalian cells is mediated by TRPT1 and multiple PARPs. *Nucleic Acids Res.*, **50**, 9426–9441.
12. Weixler,L., Scharinger,K., Momoh,J., Luscher,B., Feijs,K.L.H. and Zaja,R. (2021) ADP-ribosylation of RNA and DNA: from in vitro characterization to in vivo function. *Nucleic Acids Res.*, **49**, 3634–3650.
13. Munir,A., Banerjee,A. and Shuman,S. (2018) NAD+-dependent synthesis of a 5'-phospho-ADP-ribosylated RNA/DNA cap by RNA 2'-phosphotransferase Tpt1. *Nucleic Acids Res.*, **46**, 9617–9624.

14. Culver,G.M., McCraith,S.M., Consaul,S.A., Stanford,D.R. and Phizicky,E.M. (1997) A 2'-phosphotransferase implicated in tRNA splicing is essential in *Saccharomyces cerevisiae*. *J. Biol. Chem.*, **272**, 13203–13210.
15. Remus,B.S. and Shuman,S. (2013) A kinetic framework for tRNA ligase and enforcement of a 2'-phosphate requirement for ligation highlights the design logic of an RNA repair machine. *RNA*, **19**, 659–669.
16. McCraith,S.M. and Phizicky,E.M. (1991) An enzyme from *Saccharomyces cerevisiae* uses NAD+ to transfer the splice junction 2'-phosphate from ligated tRNA to an acceptor molecule. *J. Biol. Chem.*, **266**, 11986–11992.
17. Steiger,M.A., Jackman,J.E. and Phizicky,E.M. (2005) Analysis of 2'-phosphotransferase (Tpt1p) from *Saccharomyces cerevisiae*: evidence for a conserved two-step reaction mechanism. *RNA*, **11**, 99–106.
18. Banerjee,A., Munir,A., Abdullahu,L., Damha,M.J., Goldgur,Y. and Shuman,S. (2019) Structure of tRNA splicing enzyme Tpt1 illuminates the mechanism of RNA 2'-PO4 recognition and ADP-ribosylation. *Nat. Commun.*, **10**, 218.
19. Tromans-Coia,C., Sanchi,A., Moeller,G.K., Timinszky,G., Lopes,M. and Ahel,I. (2021) TARG1 protects against toxic DNA ADP-ribosylation. *Nucleic Acids Res.*, **49**, 10477–10492.
20. Kabsch,W. (2010) Xds. *Acta Crystallogr. D Biol. Crystallogr.*, **66**, 125–132.
21. McCoy,A.J., Grosse-Kunstleve,R.W., Adams,P.D., Winn,M.D., Storoni,L.C. and Read,R.J. (2007) Phaser crystallographic software. *J. Appl. Crystallogr.*, **40**, 658–674.
22. Adams,P.D., Afonine,P.V., Bunkoczi,G., Chen,V.B., Davis,I.W., Echols,N., Headd,J.J., Hung,L.W., Kapral,G.J., Grosse-Kunstleve,R.W. *et al.* (2010) PHENIX: a comprehensive Python-based system for macromolecular structure solution. *Acta Crystallogr. D Biol. Crystallogr.*, **66**, 213–221.
23. Emsley,P., Lohkamp,B., Scott,W.G. and Cowtan,K. (2010) Features and development of Coot. *Acta Crystallogr. D Biol. Crystallogr.*, **66**, 486–501.
24. Baker,N.A., Sept,D., Joseph,S., Holst,M.J. and McCammon,J.A. (2001) Electrostatics of nanosystems: application to microtubules and the ribosome. *Proc. Natl Acad. Sci. USA*, **98**, 10037–10041.
25. Van Der Spoel,D., Lindahl,E., Hess,B., Groenhof,G., Mark,A.E. and Berendsen,H.J. (2005) GROMACS: fast, flexible, and free. *J. Comput. Chem.*, **26**, 1701–1718.
26. Lindorff-Larsen,K., Piana,S., Palmo,K., Maragakis,P., Klepeis,J.L., Dror,R.O. and Shaw,D.E. (2010) Improved side-chain torsion potentials for the Amber ff99SB protein force field. *Proteins*, **78**, 1950–1958.
27. Alphonse,S., Banerjee,A., Dantuluri,S., Shuman,S. and Ghose,R. (2021) NMR solution structures of *Runella slithyformis* RNA 2'-phosphotransferase Tpt1 provide insights into NAD+ binding and specificity. *Nucleic Acids Res.*, **49**, 9607–9624.
28. Schwer,B., Sawaya,R., Ho,C.K. and Shuman,S. (2004) Portability and fidelity of RNA-repair systems. *Proc. Natl Acad. Sci. USA*, **101**, 2788–2793.
29. Chandrashekar,D.S., Bashel,B., Balasubramanya,S.A.H., Creighton,C.J., Ponce-Rodriguez,I., Chakravarthi,B. and Varambally,S. (2017) UALCAN: a portal for facilitating tumor subgroup gene expression and survival analyses. *Neoplasia*, **19**, 649–658.
30. Kato-Murayama,M., Bessho,Y., Shirouzu,M. and Yokoyama,S. (2005) Crystal structure of the RNA 2'-phosphotransferase from *Aeropyrum pernix* K1. *J. Mol. Biol.*, **348**, 295–305.
31. Sawaya,R., Schwer,B. and Shuman,S. (2005) Structure–function analysis of the yeast NAD+-dependent tRNA 2'-phosphotransferase Tpt1. *RNA*, **11**, 107–113.
32. Hottiger,M.O., Hassa,P.O., Luscher,B., Schuler,H. and Koch-Nolte,F. (2010) Toward a unified nomenclature for mammalian ADP-ribosyltransferases. *Trends Biochem. Sci.*, **35**, 208–219.
33. Harada,K. and Frankel,A.D. (1995) Identification of two novel arginine binding DNAs. *EMBO J.*, **14**, 5798–5811.
34. Raman,B., Guarnaccia,C., Nadassy,K., Zakhariev,S., Pintar,A., Zanuttin,F., Frigyes,D., Acatrinei,C., Vindigni,A., Pongor,G. *et al.* (2001) N(omega)-arginine dimethylation modulates the interaction between a Gly/Arg-rich peptide from human nucleolin and nucleic acids. *Nucleic Acids Res.*, **29**, 3377–3384.
35. Ukmar-Godec,T., Hutten,S., Grieshop,M.P., Rezaei-Ghaleh,N., Cima-Omori,M.S., Biernat,J., Mandelkow,E., Soding,J., Dormann,D. and Zweckstetter,M. (2019) Lysine/RNA-interactions drive and regulate biomolecular condensation. *Nat. Commun.*, **10**, 2909.
36. Karlberg,T., Klepsch,M., Thorsell,A.G., Andersson,C.D., Linusson,A. and Schuler,H. (2015) Structural basis for lack of ADP-ribosyltransferase activity in poly(ADP-ribose) polymerase-13/zinc finger antiviral protein. *J. Biol. Chem.*, **290**, 7336–7344.
37. Alemasova,E.E. and Lavrik,O.I. (2019) Poly(ADP-ribosyl)ation by PARP1: reaction mechanism and regulatory proteins. *Nucleic Acids Res.*, **47**, 3811–3827.
38. Aravind,L., Zhang,D., de Souza,R.F., Anand,S. and Iyer,L.M. (2015) The natural history of ADP-ribosyltransferases and the ADP-ribosylation system. *Curr. Top. Microbiol. Immunol.*, **384**, 3–32.
39. Kleine,H., Poreba,E., Lesniewicz,K., Hassa,P.O., Hottiger,M.O., Litchfield,D.W., Shilton,B.H. and Luscher,B. (2008) Substrate-assisted catalysis by PARP10 limits its activity to mono-ADP-ribosylation. *Mol. Cell*, **32**, 57–69.
40. Munnur,D. and Ahel,I. (2017) Reversible mono-ADP-ribosylation of DNA breaks. *FEBS J.*, **284**, 4002–4016.
41. Notredame,C., Higgins,D.G. and Heringa,J. (2000) T-Coffee: a novel method for fast and accurate multiple sequence alignment. *J. Mol. Biol.*, **302**, 205–217.
42. Robert,X. and Gouet,P. (2014) Deciphering key features in protein structures with the new ENDscript server. *Nucleic Acids Res.*, **42**, W320–W324.